DESIGN AND EXPERIMENT OF SELF-PROPELLED SYSTEM FOR PADDY FIELD WEEDER BASED ON THE INTERACTION MECHANISM OF WHEEL-SOIL

Liang Tian[1], Chengmao Cao[1*,2], Kuan Qin[1*,2], Jun Ge[1,2], Liangfei Fang[1]

[1*]Corresponding author. Anhui Agricultural University/ Hefei, China.
E-mail: caochengmao@sina.com | ORCID ID: https://orcid.org/0000-0002-0505-4994
E-mail: qinkuan@ahau.edu.cn| ORCID ID: https://orcid.org/0000-0002-4411-9631

ABSTRACT

Aiming at the low mechanization of paddy field weeding and lack of dedicated agricultural machinery for paddy field weeding in China, a self-propelled system of paddy field weeding machine was designed. The overall structure and working principle of self-propelled system were illustrated and analyzed. The interaction mechanism of wheel-soil during weeding was analyzed. The wheel-soil interaction model was established, then, wheel traction and surface flatness were selected as the evaluation indexes for discrete element simulation experiment. The steering performance, stability, and over ridge ability of self-propelled system were analyzed, and field experiment was carried out. The simulation experiment results show that the wheel traction is approximately 600 N and the surface flatness is less than 30 mm. The field experiment results show that the minimum turning radius of the prototype is 2,050 mm in paddy, overturning limit angle of the prototype is 36º, and maximum height over the ridge is 400 mm. The speed range of the weeding machine on the road and weeding operation was 0~16.20 km/h and the 0~5.40 km/h respectively. The weeder can meet the speed demands of weeding operation. The study results can provide reference for research and development of paddy field operation machinery.

INTRODUCTION

There are many kinds of weeds in paddy fields competing for living space with rice (Tang et al., 2018), and breeding diseases and pests, which is one of the main factors affecting rice yield. The scientific and effective control of weeds in paddy fields is the key to achieving high and excellent rice yield (Basavaraj et al., 2016; Atul et al., 2017). Mechanical weeding is an efficient and environment-friendly weeding method, which is used to remove weeds in the field, loosen the soil, and promote plant growth (He et al., 2018; Qi et al., 2017; Tian et al., 2021).

There are many research achievements on paddy field weeding machinery in Japan (Wang et al., 2017 a; Qi et al., 2016). The SJ-6N riding weeding machine (Ma et al.,

2011) developed by Kubota company has high operation efficiency and a good weeding effect. The walking weeding machine in paddy fields (Qi et al., 2012) developed by Meishan Co., Ltd. has flexible steering, but its working efficiency is not high. Chinese scholars have also carried out a series of research on paddy field weeding machinery. The organic rice weeding machine (Wang et al., 2018; Tao et al., 2015) designed by Wang Jinwu could cover multiple rows in weeding operations with a high operation efficiency; however, it required supporting traction machinery, a large turning radius, and crushed seedlings. The hand-held weeder (Qi et al., 2013; Qi et al., 2015) developed by Qilong has a compact structure and flexible field steering, but low work efficiency and high labor intensity.

[1] School of Engineering, Anhui Agricultural University/ Hefei, China.
[2] Scientific observing and experimental Station of Agricultural Equipment for the Southern China/ Ministry of Agriculture and Rural Affairs of the People's Republic of China/ Hefei, China.

To improve the trafficability and working efficiency of the paddy field weeder and reduce the damage to seedlings, the design and experimental research of a paddy field weeder self-propelled system were carried out. Based on the analysis of the influencing factors of the trafficability of the machine, an interaction model between the driving wheel of the weeder and paddy soil was established, and a discrete element simulation experiment was carried out to explore the change law of the mechanical characteristics of the wheel and soil during the contact process of the weeder. To verify the rationality of the self-propelled system design, a field experiment was carried out on the prototype of the weeder to test the stability and steering performance of the weeder. This study can provide a reference for research on the paddy field operation machinery self-propelled system.

MATERIAL AND METHODS

Overall design of self-propelled system of paddy field weeder

Design requirements

The paddy field environment is complex and diverse, which requires high maneuverability and trafficability operation machinery (Wang et al., 2017 b), to meet the requirements of strong climbing and ridge crossing ability, a high ground gap, and small wheel sinking in the operation process, to realize the paddy field weeding operation. The purpose of this study is to design a self-propelled system for the paddy field weeding machine for efficient and high quality weeding. To ensure that the weeder can adapt to different paddy field environments, and

that it has the characteristics of smooth driving, a small turning radius, and a low seedling injury rate, considering the domestic rice planting agronomy, the requirements of the self-propelled system of the weeder were determined as follows:

1) The steering should be flexible, and the turning radius of the machine should be small when turning around in the field, to avoid rolling on seedlings by the wheel, and reduce seedling damage.

2) The speed adjustment range should be wide to meet the speed requirements of field working and road driving.

3) The trafficability should be strong with a strong climbing ability and good stability, to cross ridges and facilitate driving on slopes.

4) The working effect should be visible, which makes it convenient for the driver to move in time according to the operation situation and reduces the damage of seedlings.

5) The adaptability should be strong with a high working efficiency, enough chassis height, and load-bearing capacity. During the weeding operation, the weeder chassis passes over the seedlings, and the driver rides on the weeding machine with a high clearance chassis to ensure that the machine does not crush the seedlings during operation.

Overall technical route

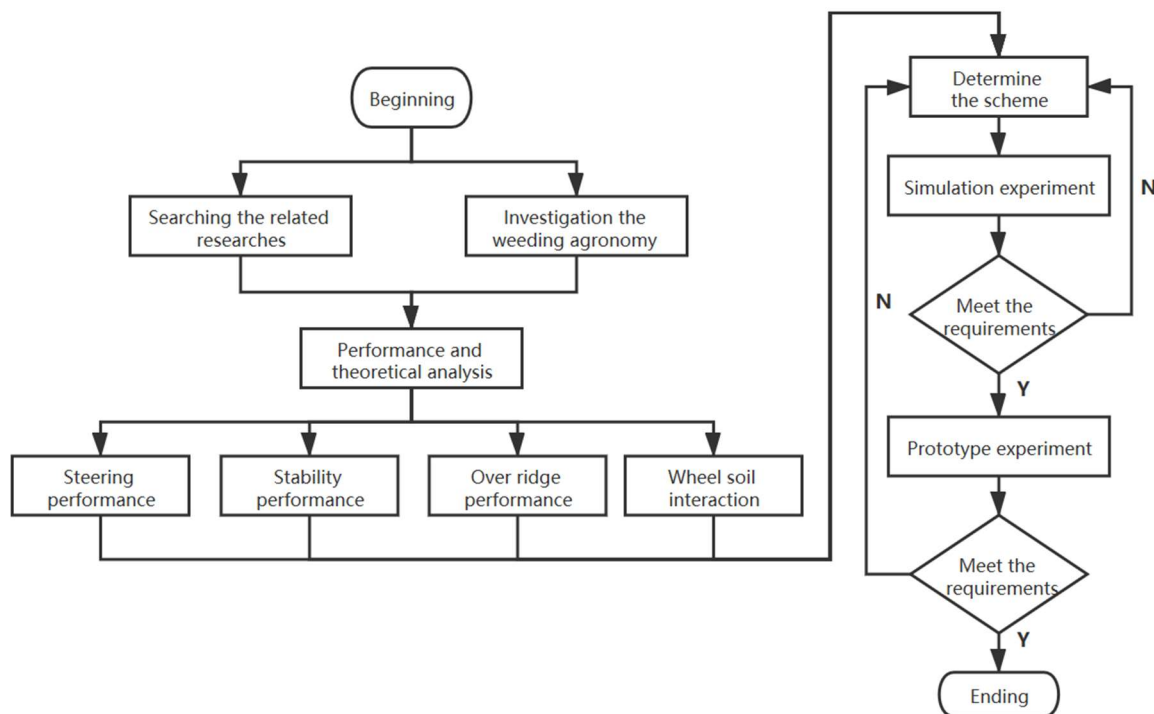The technical route of the self-propelled system of the paddy field weeder is shown in Figure 1.

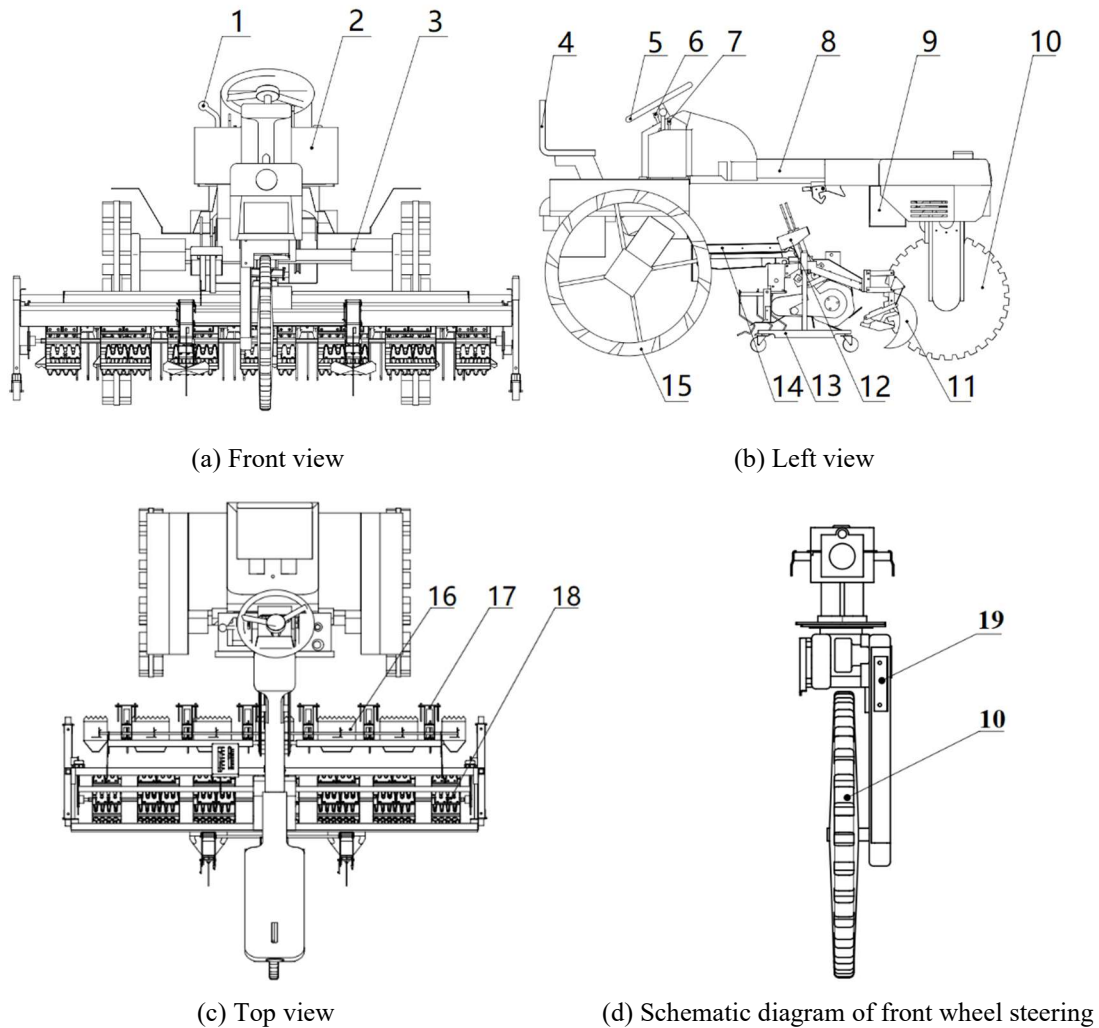FIGURE 1. Technical route of self-propelled system for paddy field weeder.

Overall structure

(a) Front view

(b) Left view

(c) Top view

(d) Schematic diagram of front wheel steering

FIGURE 2. Schematic diagram of the paddy field weeding machine.

Note:1. Working speed adjusting rod 2. Oil tank 3. Axle 4. Seat 5. Steerable wheel 6. Working state adjusting rod 7. Hydraulic lifting rod 8. Frame 9. Battery 10. Front wheel 11. Depth limiting and anti entanglement device 12. Weeding depth adjusting device 13. Auxiliary walking device 14. Suspension device 15. Rear wheel 16. Mud covering device 17. Intra-row weeding device 18. Inter-row weeding device 19. Front wheel suspension system.

As shown in Figure 2, the paddy field weeding machine is mainly composed of a frame, front wheel, rear wheel, inter-row weeding device, intra-row weeding device, weeding depth adjusting device, suspension device, mud covering device, and related accessories. To reduce damage to the seedlings while weeding, three wheels riding weeding machine was designed. The weeding machine steering and driving were by the front wheel, to reduce the turning radius, and seedling damage.

Working principle

The paddy field weeding machine is powered by a gasoline engine; one part power is for walking, and the other part is used for weeding. Before the weeding operation, the driver should row-control and adjust the working parameters of the weeder according to the weeding environment and seedling growth status.

When the paddy field weeding machine is working, the entire machine straddles over the rice seedlings, the wheels running between the rows, and it moves in a straight line. Figure 3 is the schematic diagram of the weeding machine during operation. When the wheel of the paddy field weeding machine moves forward in the soft paddy soil, it is easy to slip and sink, and the driving track deviates, which affects its working efficiency and weeding rate, causes seedling damage, and severely affects the operation performance of the machine. It is necessary for the driver to correct the forward direction of the machine in time.
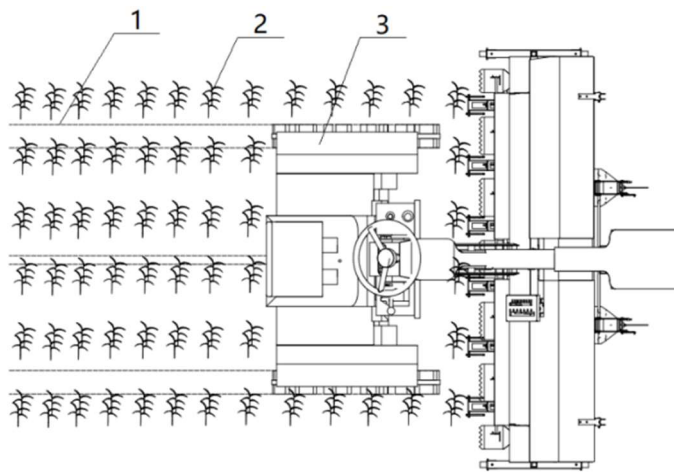
FIGURE 3. Schematic diagram of the paddy field weeding machine operation.

Note:1. Walking track 2. Rice seedling 3. Paddy field weeding machine.

To reduce the slippage of the machine, restrict the sinking depth, improve the wheel grip (Zhao et al., 2016), improve the traction efficiency of the machine, and reduce the scratch of the chassis on the seedlings, the narrow section steel reinforced deep tread rubber tire is selected as the wheels of the weeding machine. The seat was set at the rear so that the driver could observe the operation of the machine, reduce the deflection of the driving track, and ensure the operation efficiency of the machine. To ensure that the machine runs smoothly (Chen et al., 2012), and improve the driving comfort and steering flexibility, the wheelbase of the self-propelled system is set as 1,700 mm and the wheelbase is 1,320 mm.

Main technical parameters

1) Prototype dimension (Length × Width × Height): 2,700 mm × 1,400 mm × 1,500 mm

2) Mass: 300 kg

3) Gasoline engine power: 7.5 kw

4) Track width: 1,320 mm

5) Wheelbase: 1,700 mm

6) Front wheel diameter: 680 mm

7) Rear wheel diameter: 900 mm

8) Minimum turning radius: 2,050 mm

9) Ultimate tipping angle: 36°

10) Driving speed: 0~16.20 km/h

Self-propelled system design

Design of driving wheel diameter and tire width

The ground clearance and carcass width should be reasonable to reduce seedling damage during turning. To protect the root system of the rice seedlings and avoid influencing their subsequent growth, the crop protection areas (Li et al., 2016; Sun et al., 2017 a) were set, and the weeding machine did not work in those areas.
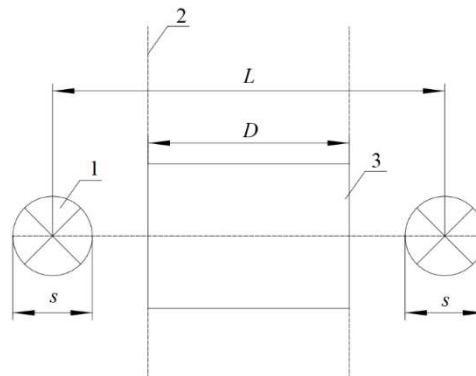

FIGURE 4. Schematic diagram of driving wheel and intra-row space while turning.

Note: 1. Crop protection area; 2. Driving track of driving wheel; 3. Driving wheel; L is the intra-row spacing of the rice, mm; D is the width of the driving wheel, mm; S is the scope of the crop protection area, mm.

Figure 4 shows the driving wheel and intra-row space while turning. When the weeder turns in the field, there should be a gap between the driving wheel and root system of the rice plant to avoid seedling damage. According to Figure 4,

$$D \leq L - S \qquad (1)$$

in which:

D－the width of the driving wheel, mm;

L－the intra-row spacing of the rice, mm,

S－the scope of the crop protection area, mm.

According to the agronomic requirements (Zhu et al., 2017), the inter-row spacing of the seedlings is 300 mm and the intra-row spacing is approximately 130 mm. According to the relevant research on rice growth (Wang et al., 2017), the distribution of rice roots at the tillering stage is generally in the range of 0~50 mm. Substituting in (1), D ≤ 80 mm is obtained, and D was set as 70 mm, which meets the design requirements.

According to the growth characteristics of rice (Bai & Yin 2017), the height of the rice seedlings was not higher than 400 mm after two weeks of transplanting. To ensure that the chassis of the weeder does not scratch the seedlings while weeding, the diameter of the driving wheel should be set reasonably.
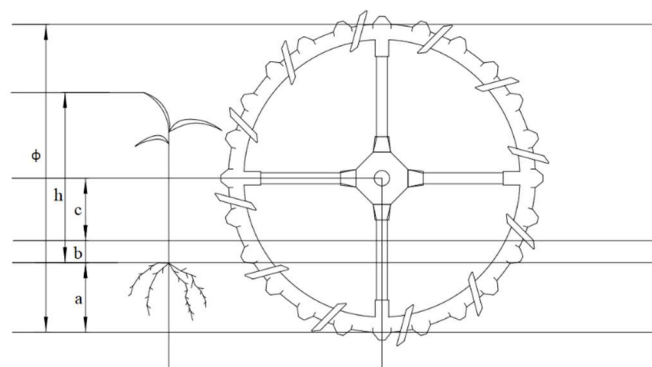

FIGURE 5. Schematic diagram of driving wheel and seedling height.

Note: ϕ is the diameter of the driving wheel, mm; h is the height of the seedling, mm; a is the sinking depth of the driving wheel, mm; b is the water depth of the paddy, mm; and c is the distance between the water surface and wheelbase, mm.

Figure 5 is a schematic diagram of the height between the driving wheel and seedling during weeding. When the weeder is working in the paddy, the seedling height should be lower than the chassis of the machine. According to Figure 5, the equation is as follows:

$$\begin{cases} \phi = 2(a+b+c) \\ \phi > h+a \end{cases} \qquad (2)$$

in which:

ϕ — the diameter of the driving wheel, mm;

h — the height of the seedling, mm;

a — the sinking depth of the driving wheel, mm;

b — the water depth of the paddy, mm,

c — the distance between the water surface and wheelbase, mm.

According to the soil characteristics of the paddy field (Fu 2018; Xie & Gao 2016), the wheel sinking depth is not more than 200 mm. In this study, a is 200 mm, b is 30 mm, h is 400 mm, and $c > 70$ mm can be obtained from (2). To avoid the contact between the drive wheel suspension system and water surface, c is set as 220 mm; the value of ϕ value could then be calculated as 900 mm.

Steering mechanism design

The steering system is a series of devices used to change or maintain the driving or reversing direction of the vehicle. The steering mode of the front wheel drive is adopted, and its structural diagram is shown in Figure 6.
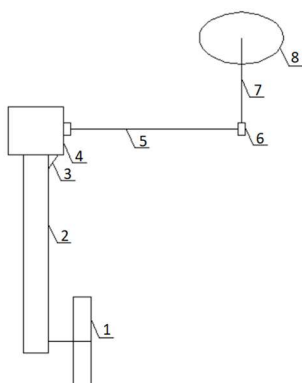

FIGURE 6. Schematic diagram of steering system.

Note: 1. Steerable wheel; 2. Steerable wheel suspension; 3. Steering rocker rod; 4. Steering gear; 5. Steering transmission shaft; 6. Steering universal joint; 7. Steering shaft; 8. Steering wheel.

When the machine is in operation, the driver exerts the steering torque to the steering wheel, which is input into the steering gear through the steering shaft, steering universal joint, and steering transmission shaft. The amplified torque and motion of the steering gear are transmitted to the steering rocker rod, which drives the

steerable wheel suspension and steerable wheel supported by it to deflect and realize the turning of the weeding machine.

Power output distribution

The weeder is powered by a gasoline engine. The engine power is distributed into three parts: the weeding system, hydraulic take-off system, and walking system. The power output distribution route is shown in Figure 7.
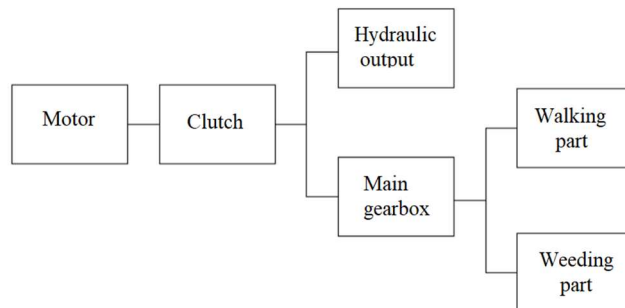

FIGURE 7. Schematic diagram of power output distribution route.

The engine power is transmitted to the hydraulic output system and the main gearbox through the clutch, and the hydraulic output system drives the lifting of the weeding parts. The power transmitted by the main gearbox is divided into two parts. One part distributes the power to the driving wheels through the central transmission and gearbox to drive the machines and tools to walk. The other part distributes the power to the external weeding parts through the power output shaft and gearbox to implement the weeding operation.

Weeder performance analysis and interaction mechanism of wheel-soil study

Steering performance analysis

There are at least two steerable wheels in a four-wheel vehicle. When turning, the rolling distance of the inner wheel and outer wheel is not equal, which causes the simultaneous rolling and sliding of the wheels along the road; the driving resistance and wheel wear is then increased (Wang et al., 2019). To avoid these conditions and make the wheels roll only, it is necessary to follow the Ackerman steering principle (Kwangseok et al., 2017; Zhang et al., 2015; Qin et al., 2014). That is, when the vehicle turns, all wheel axes should intersect at one point. Three-wheel vehicle has the advantages of compact structure, flexible steering, good road trafficability, easy operation and low cost. It has become a common model of agricultural vehicles.

The self-propelled system of the weeder adopts the three-wheel structure, with the front wheel steering and rear wheel drive. When turning, the front and rear wheel axes intersect at a point, and the steerable wheel achieves pure rolling, which reduces tire wear and steering resistance. Figure 8 is the turning diagram of the three-wheel paddy weeder on flat ground.
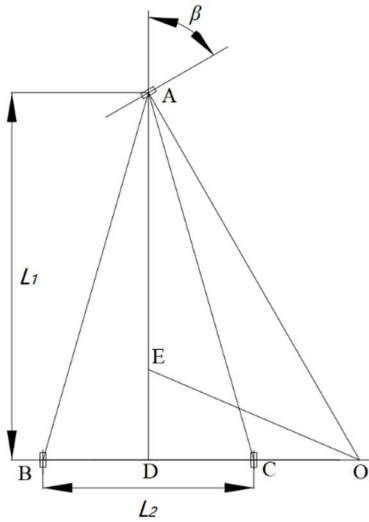
FIGURE 8. Schematic diagram of the steering of the paddy field weeding machine.

Note: A is the front wheel; B is the left rear wheel; C is the right rear wheel; D is the midpoint of BC; E is the center of gravity of the weeder; O is the turning center; β is the front wheel turning angle (°); L_1 is the wheelbase, mm; and L_2 is the track width, mm.

According to the geometric relationship in Figure 8,

$$\begin{cases} OD = AD \cot \beta \\ OA = \sqrt{OD^2 + AD^2} \\ OB = OD + \dfrac{1}{2} BC \end{cases} \qquad (3)$$

in which:

AD－the wheelbase of the weeder, mm;

OA－the turning radius of the front wheel of the weeding machine, mm;

BC－the rear wheel track of the weeding machine, mm;

OB－the turning radius of the rear wheel of the weeding machine, mm,

β－the front wheel turning angle (°).

Especially, $\begin{cases} AD = L_1 \\ BC = L_2 \end{cases} \qquad (4)$

Substituting (4) into (3), we obtain

$$\begin{cases} OA = L_1 \sqrt{1 + \cot^2 \beta} \\ OB = L_1 \cot \beta + \dfrac{1}{2} L_2 \end{cases} \qquad (5)$$

From (5), the turning radius of the weeder is related to the rear wheelbase of L_1, the rear wheel distance of L_2, and the turning angle β of the front wheel. With other parameters unchanged, the front and rear wheelbase L_1 increases, the turning radius of the front wheel and rear wheel increases, and the turning ability of the weeder declines. With the increase of L_2, the turning radius of the front wheel of the machine remains unchanged, but the turning radius of the rear wheel of the machine increases, and the turning ability of the entire machine declines; the front wheel turning angle β increases, the turning radius of the front wheel and rear wheel of the implement increases, and the turning ability of the weeder is enhanced.

To meet the walking requirements of the paddy field operation, the front wheel deflection angle is set to be 0~60°. According to the structural parameters of the weeder, the wheelbase L_1 is 1,700 mm, and the wheelbase L_2 is 1,320 mm. When the front wheel turning angle β is 60°, the turning radius of the front wheel of the weeder is 1,963 mm and that of the rear wheel is 1,642 mm, that is, the minimum turning radius of the weeder is 1,963 mm. This meets the turning radius requirements of general machines and tools for paddy field operation.

Stability analysis

When the weeder works in the field, the field conditions are complex, thus, the driving stability of the machine should be considered. The driving stability of the machine is measured by the longitudinal stability (Editorial Department of China Journal of highway and transport 2016). When the weeder runs or stops on the ramp, the stability of the self-propelled system of the weeder is evaluated by the maximum slope angle without overturning and sliding.

When the weeder runs on the ramp at a constant speed, it can be regarded as parking at rest on the ramp owing to the low speed uphill and downhill. Ignoring the air resistance and tire and ground deformation, the force analysis of the self-propelled system of the weeder was carried out.
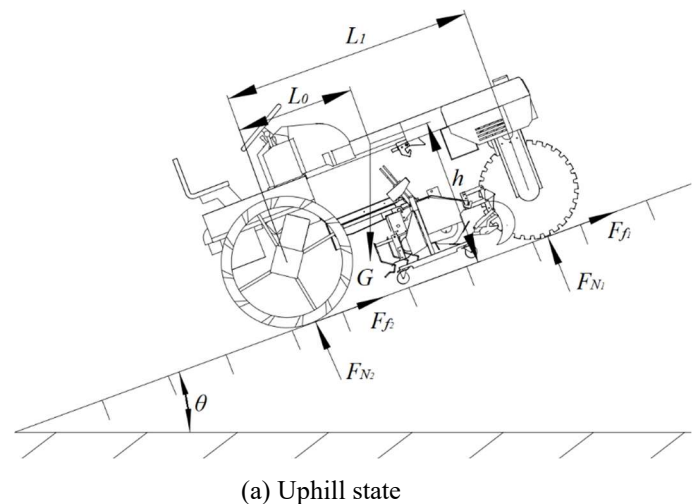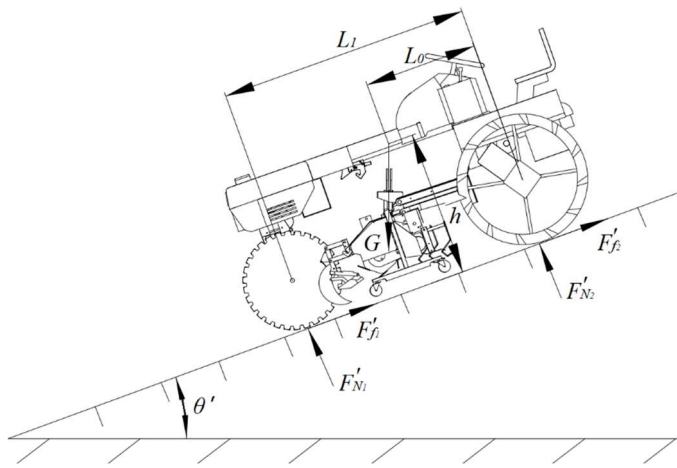
(a) Uphill state

(b) Downhill state

FIGURE 9. Schematic diagram of longitudinal limit tiling state of weeding machine.

Note: θ is the maximum turning angle uphill, (°); F_{N_1} is the normal force of the front wheel uphill, N; F_{f_1} is the forward tangential force of the front wheel uphill, N; F_{N_2} is the normal force of the rear wheel uphill, N; F_{f_2} is the forward tangential force of the rear wheel uphill, N; G is the gravity of the weeding machine, N; L_1 is the wheelbase, mm ; L_0 is the distance between the center of gravity of the weeding machine and the rear axle, mm; h is the vertical height of the weeding machine to the ground, mm; $\theta^{'}$ is the maximum turning angle downhill, (°); $F_{N_1}^{'}$ is the normal force of the front wheel downhill, N; $F_{f_1}^{'}$ is the forward tangential force of the front wheel downhill, N; $F_{N_2}^{'}$ is the normal force of the rear wheel downhill, N; and $F_{f_2}^{'}$ is the forward tangential force of the rear wheel downhill, N.

The force analysis of the uphill state of the weeder is shown in Figure 9a. The following equation is obtained:

$$\begin{cases} F_{f_1} + F_{f_2} = G \sin\theta \\ F_{N_1} + F_{N_2} = G \cos\theta \\ F_{N_1} L_1 + Gh \sin\theta = GL_0 \cos\theta \end{cases} \quad (6)$$

in which:

F_{f_1}—the tangential force of the soil on the front wheel of the weeder going uphill, N;

F_{f_2}—the tangential force of the soil on the rear wheel of the weeder uphill, N;

F_{N_1}—the normal force of the soil on the front wheel of the weeder going uphill, N;

F_{N_2}—the normal force of the soil on the rear wheel of the weeder going uphill, N;

G—the total gravity of the weeder and driver during operation, N;

θ—the ultimate turning angle uphill (°);

h—the vertical height from the center of gravity of the weeder to the ground, mm;

L_1—the front and rear wheel track of the weeder, mm;

L_0—the distance from the center of gravity of the weeder to the rear axle, mm.

When the weeder is in the critical state of uphill tipping, the soil force on the front wheel is zero. Therefore,

$$\begin{cases} F_{f_1} = 0 \\ F_{N_1} = 0 \end{cases} \quad (7)$$

Substituting (7) into (6), we obtain,

$$\theta = arctan \frac{L_0}{h} \quad (8)$$

From (8), the maximum turning angle of the weeder going uphill is related to the position of the center of gravity of the entire machine. The larger the ratio of the distance between the center of gravity and height of the center of gravity of the weeder, the greater the ultimate inclination angle of the weeder uphill, and the stronger the stability.

In the same way, the mechanical analysis of the downhill state of the weeder is carried out, as shown in Figure 9b. The following equation is obtained:

$$\begin{cases} F_{f_1}^{'} + F_{f_2}^{'} = G \sin\theta^{'} \\ F_{N_1}^{'} + F_{N_2}^{'} = G \cos\theta^{'} \\ F_{N_2}^{'} L_1 + Gh \sin\theta^{'} = G(L_1 - L_0)\cos\theta^{'} \end{cases} \quad (9)$$

in which:

$F_{f_1}^{'}$ and $F_{f_2}^{'}$—the tangential forces of the soil on the front and rear wheels of the weeder, respectively, going downhill, N;

$F_{N_1}^{'}$ and $F_{N_2}^{'}$—the normal forces of the soil on the front and rear wheels of the weeder, respectively, going downhill, N,

$\theta^{'}$—the ultimate turning angle downhill (°).

When the weeder is in the critical state of downhill tipping, the soil force on the rear wheel is zero. That is,

$$\begin{cases} F_{f_2}^{'} = 0 \\ F_{N_2}^{'} = 0 \end{cases} \quad (10)$$

Substituting (9) into (10), it can be gotten that:

$$\theta^{'} = arctan \frac{L_1 - L_0}{h} \quad (11)$$

From (11) it can be observed that the ultimate downhill turning angle of the weeder is related to the position of the center of gravity of the entire machine. The larger the ratio of the distance from the center of gravity to the front axle and height of the center of gravity of the weeder, the greater the downhill turning angle and the stronger the downhill ability.

From (8) and (11), to enhance the driving stability of the weeder, the structure parameters of the weeder should be set reasonably, and the center of gravity of the weeder should not be too high.

It is assumed that the height of the driver is 1.75 m and the mass is 75 kg during the operation of the weeding machine. The three-dimensional model of the weeder is introduced into UG software for analysis and measurement, and the center of gravity position of the overall machine is obtained. The vertical height h from the center of gravity of the weeder to the ground is 700 mm, and the distance from the center of gravity of the weeder to the rear axle L_0 is 750 mm. The above parameters are substituted into (8) and (11), and the ultimate slope turning angle of the mower is 43.9°. The ultimate turning angle of the weeder downhill is 50.7°.

Performance analysis of ridge crossing

When weeding in the field, the weeder needs to frequently cross ridges. Ridge crossing performance is an important index to evaluate the field trafficability of the weeder (Hao et al., 2018). The ridge crossing height was selected as the index to analyze the ridge crossing performance of the weeder. The driving speed of the weeder is not high when it crosses the ridge. The ridge crossing model is simplified as a static problem, and the force analysis of the front and rear wheels of the weeder is carried out. Figure 10 is a schematic diagram of the ridge crossing state of the weeder.
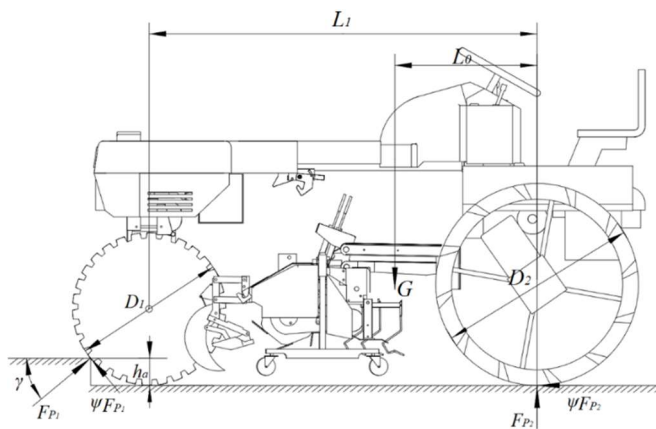
(a) Climbing ridge state of front wheel
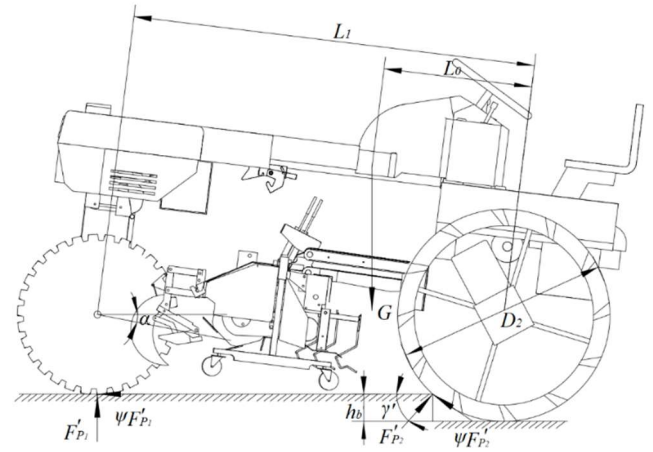
(b) Climbing ridge state of rear wheel

FIGURE 10. Schematic diagram of wheel crossing of the weeding machine.

Note: F_{P_1} is the normal force of the front wheel when climbing the ridge, N; ψF_{P_1} is the forward tangential force of the front wheel when climbing the ridge, N; h_a is the ridge height when the front wheel is climbing the ridge, mm; γ is the angle between the normal force of the front wheel and the horizontal plane when the front wheel is climbing the ridge, (°); F_{P_2} is the normal force of the front wheel when climbing the ridge, N; ψF_{P_2} is the forward tangential force of the front wheel when climbing the ridge, N; D_1 is the diameter of the front wheel, mm; D_2 is the diameter of the rear wheel, mm; F'_{P_1} is the normal force of the front wheel when the rear wheel is climbing the ridge, N; $\psi F'_{P_1}$ is the forward tangential force of the front wheel when the rear wheel is climbing the ridge, N; h_b is the ridge height when the rear wheel is climbing the ridge, mm; γ' is the angle between the normal force of the front wheel and the horizontal plane when the rear wheel is climbing the ridge, (°); α is the normal force of the field ridge on the back wheel of the weeding machine when the rear wheel is climbing the ridge, N; F'_{P_2} is the normal force of the front wheel when the rear wheel is climbing the ridge, N; and $\psi F'_{P_2}$ is the the forward tangential force of the front wheel when the rear wheel is climbing the ridge, N.

When the front wheel of the weeding machine is climbing the ridge, the driving speed of the machine is not high, and the air resistance can be ignored. The entire machine is approximately in the equilibrium state. The force analysis of the weeder is shown in Figure 10a. Ignoring the elastic deformation of the tire, we obtain

$$\begin{cases} F_{P_1} \sin\gamma + \psi F_{P_1} \cos\gamma + F_{P_2} = G \\ F_{P_1} \cos\gamma = \psi F_{P_1} \sin\gamma + \psi F_{P_2} \\ \psi F_{P_1} D_1 / 2 + \psi F_{P_2} D_1 / 2 + G(L_1 - L_0) = F_{P_2} L_1 \end{cases} \quad (12)$$

in which:

ψ — the soil adhesion coefficient;

F_{P_1} — the normal force of the ridge on the front wheel of the weeder when the front wheel of the weeder crosses the ridge, N;

ψF_{P_1} — the tangential force of the ridge on the front wheel of the weeder when the front wheel of the weeder crosses the ridge, N;

γ — the angle between the normal force of the ridge on the front wheel of the weeder and the horizontal plane when the front wheel of the weeder crosses the ridge (°)；

F_{P_2} — the normal force of the ridge on the rear wheel of the weeder when the front wheel of the weeder crosses the ridge, N;

ψF_{P_2} — the tangential force of the ridge on the rear wheel of the weeder when the front wheel of the weeder crosses the ridge, N;

D_1 — the diameter of the front wheel of weeder, mm. Subsequently, (12) can be simplified as:

$$cos\,\gamma\left(\frac{D_1}{2L_1}+\frac{L_1-L_0}{L_1}\frac{\psi^2+1}{\psi}-\frac{1}{\psi}\right)-sin\,\gamma\left(\frac{D_1\psi}{2L_1}+1\right)+\frac{D_1\psi}{2L_1}=0 \tag{13}$$

According to the geometric relationship in Figure 10a, it can be deduced that:

$$sin\,\gamma = 1-\frac{2h_a}{D_1} \tag{14}$$

in which:

h_a — the height of the front wheel of the weeder over the ridge, mm.

Substituting (14) into (13) yields

$$h_a = \frac{D_1}{2}\left[1-\sqrt{\left(\frac{bc}{a^2+b^2}\right)^2+\frac{b^2-c^2}{a^2+b^2}}+\frac{bc}{a^2+b^2}\right] \tag{15}$$

Especially,
$$\begin{cases} a = \dfrac{D_1\psi}{2L_1}+\dfrac{L_1-L_0}{L_1}\dfrac{\psi^2+1}{\psi}-\dfrac{1}{\psi} \\[2mm] b = \dfrac{D_1\psi}{2L_1}+1 \\[2mm] c = -\dfrac{D_1\psi}{2L_1} \end{cases} \tag{16}$$

From (15), the height of the front wheel crossing of the grass weeder h_a is related to the diameter of the front wheel D_1, the soil adhesion coefficient ψ, the wheelbase between the front and rear wheels L_1, and the distance from the center of gravity of the weeding machine to the front wheel L_1-L_0.

In the same way, the force analysis of the rear wheel over the ridge state of the weeder was carried out. When the rear wheel of the weeder crosses the ridge, the driving speed of the machine is low, the air resistance can be ignored, and the entire machine is approximately in a balanced state, as shown in Figure 10b. Ignoring the elastic deformation of the tire, the mechanical equilibrium equation is established:

$$\begin{cases} F'_{P_1}+F'_{P_2}\,sin\,\gamma'+\psi F'_{P_2}\,cos\,\gamma' = G \\ \psi F'_{P_1}+\psi F'_{P_2}\,sin\,\gamma' = F'_{P_2}\,cos\,\gamma' \\ F'_{P_1}L_1\,cos\,\alpha+\psi F'_{P_1}(D_2/2-h_b)+\psi F'_{P_2}D_2/2 = GL_0\,cos\,\alpha \end{cases} \tag{17}$$

in which:

F'_{P_1} and $\psi F'_{P_1}$ — the normal and tangential forces of the ridge on the front wheel of the weeder when the rear wheel of the weeder crosses the ridge, respectively, N;

h_b — the ridge height of the rear wheel of the weeder, mm;

γ' — the angle between the normal force of the ridge on the rear wheel of the weeder and the horizontal plane when the rear wheel of the weeder crosses the ridge (°);

α — the rising angle of the entire machine when the rear wheel of the weeder crosses the ridge (°);

F'_{P_2} and $\psi F'_{P_2}$ — the normal and tangential forces of the ridge, respectively, on the rear wheel of the weeder when the rear wheel of the weeder crosses the ridge, N,

D_2 — the diameter of the rear wheel of the weeder, mm.

Then, (17) can be simplified as

$$[(\frac{1}{\psi} - \frac{\psi^2+1}{\psi}\frac{L_0}{L_1})cos\,\alpha + \frac{1}{L_1}(\frac{D_2}{2} - h_b)]\,cos\,\gamma' - [cos\,\alpha + \frac{\psi}{L_1}(\frac{D_2}{2} - h_b)]\,sin\,\gamma' + \frac{D_2\psi}{2L_1} = 0 \tag{18}$$

From the geometric relationship in Figure 10b, it can be deduced that:

$$\begin{cases} sin\,\alpha = \dfrac{h_b}{L_1} \\ \\ sin\,\gamma' = 1 - \dfrac{2h_b}{D_2} \end{cases} \tag{19}$$

From (18), it can be observed that the height of the ridge crossing of the rear wheel of the weeder h_b is related to the diameter of the rear wheel of the weeder D_2, the soil adhesion coefficient ψ, the wheelbase of the front and rear wheels L_1, and the distance from the center of gravity of the weeder to the rear wheel L_0.

When the weeder is working, the paddy soil adhesion coefficient is 0.5, which is substituted into the structure parameters of the weeder, then the heights of the front and rear wheels over the ridge are 370 mm and 425 mm, respectively. The ability of the rear wheel is better than that of the front wheel. Generally, the ability of the front wheel is measured by the height of the front wheel. In the actual production, the height of the ridge is approximately 250 ~ 300 mm, thus, the self-propelled system designed in this study can meet the requirements of paddy field ridge crossing.

Wheel soil interaction model

Combined with previous research (Li et al., 2015; Huang et al., 2015; Ge et al., 2019; Xue et al., 2020; Bao et al., 2020), the interaction model of the driving wheel and soil during the weeder operation is shown in Figure 11.
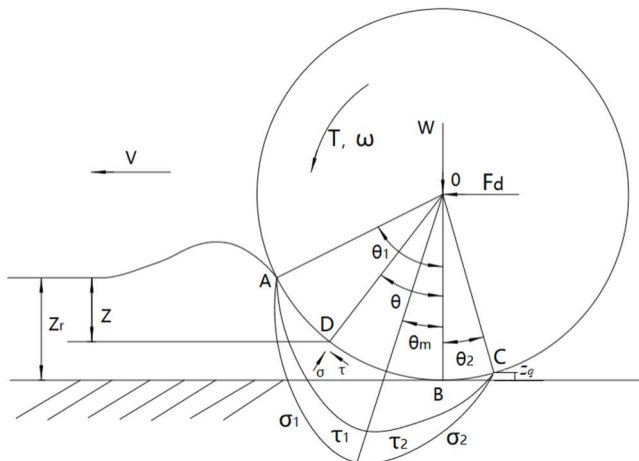

FIGURE 11. Schematic diagram of the wheel-soil interaction mechanism.

Note: θ_1 is the wheel entry angle, (°); θ_2 is the wheel departure angle, (°); θ_m is the maximum stress angle, (°); θ is the wheel-soil connection angle at any position, (°); Z_r is the height value corresponding to θ_1, mm; Z_q is the height value corresponding to θ_2, mm; Z is the wheel settlement corresponding to wheel-soil contact angle at any position, mm; σ is the normal stress of

wheel-soil contact area, MPa; σ_1 is the normal stress on the wheel entering area, MPa; σ_2 is the normal stress on the wheel leaving area, MPa; τ is the shear stress on the wheel-soil contact area, MPa; τ_1 is the shear stress on the wheel entering area, MPa; τ_2 is the shear stress on the wheel leaving area, MPa; W is the wheel load, N; T is the wheel driving torque, N·m; F_d is the wheel traction force, N; ω is the wheel rotation angular velocity, rad/s; v is the wheel driving speed, m/s; O is the wheel center; A is wheel-soil contact point corresponding to θ_1; B is the wheel-soil contact point at the lowest position of the wheel; C is the wheel soil contact point corresponding to θ_2; and D is the wheel soil contact point corresponding to the wheel soil connection angle θ at any position, mm.

The paddy soil is soft, thus, the force of the soil on the wheel is in the form of continuous stress (Chen et al., 2019), including normal stress σ and shear stress τ. The stress of the soil on the wheel is then:

$$\begin{cases} \sigma_1(\theta) = (ck_c + \gamma_s bk_\phi)(\dfrac{r}{b})^n (cos\,\theta - cos\,\theta_1)^n \\ \\ \sigma_2(\theta) = (ck_c + \gamma_s bk_\phi)(\dfrac{r}{b})^n \{cos[\theta_1 - \dfrac{\theta - \theta_2}{\theta_m - \theta_2}(\theta_1 - \theta_m)] - cos\,\theta_1\}^n \end{cases} \tag{20}$$

in which:

σ_1 — the contact normal stress between the wheel and soil in the wheel entry area, MPa;

σ_2 — the contact normal stress between the wheel and soil in the area where the wheel leaves, MPa;

θ — the wheel soil connection angle at any position (°) ;

θ_1 — the wheel entry angle (°) ;

θ_2 — the wheel leaving angle (°) ;

θ_m — the maximum stress angle (°) ;

c — soil cohesion, N;

k_c and k_φ — the dimensionless cohesive modulus and frictional deformation modulus of the soil, respectively;

γ_s — the soil bulk density, kg/m³;

b — the width of the wheel, m;

r — the wheel radius, m,

n — the subsidence deformation index of the soil.

The shear stress of the soil to the wheel is:

$$\begin{cases} \tau_1(\theta) = [c + \sigma_1(\theta)\,tan\,\varphi][1 - e^{(-j/k)}] \\ \\ \tau_2(\theta) = [c + \sigma_2(\theta)\,tan\,\varphi][1 - e^{(-j/k)}] \end{cases} \tag{21}$$

in which:

τ_1 — the contact shear stress between the wheel and soil in the wheel entry area, MPa;

τ_2 — the contact shear stress between the wheel and soil in the area where the wheel leaves, MPa;

φ — the internal friction angle of the soil (°);

c — soil cohesion, N;

j — the shear displacement of the soil, m,

k — the shear deformation modulus of the soil, MPa.

$$\begin{cases} W = rb\{ \int_{\theta_2}^{\theta_m} [\sigma_2(\theta)\cos\theta + \tau_2(\theta)\sin\theta]d\theta + \int_{\theta_m}^{\theta_1} [\sigma_1(\theta)\cos\theta + \tau_1(\theta)\sin\theta]d\theta \} \\ Fd = rb\{ \int_{\theta_2}^{\theta_m} [\tau_2(\theta)\cos\theta - \sigma_2(\theta)\sin\theta]d\theta + \int_{\theta_m}^{\theta_1} [\tau_1(\theta)\cos\theta - \sigma_1(\theta)\sin\theta]d\theta \} \\ T = br^2 [\int_{\theta_2}^{\theta_m} \tau_2(\theta)d\theta + \int_{\theta_m}^{\theta_1} \tau_1(\theta)d\theta] \end{cases} \qquad (22)$$

in which:

W — the wheel load, MPa;

T — the wheel driving torque, N·m,

F_d — the wheel traction, N.

From (22), the wheel load W, wheel driving torque T, and wheel traction F_d are related to the soil parameters and wheel structures.

The wheel sinks when moving on soft ground. Moreover, the settlement caused by the vertical load is referred to as static sinkage (Zang et al., 2014), and the subsidence caused by the wheel slip is referred to as slip sinkage (Sun et al., 2017 b).
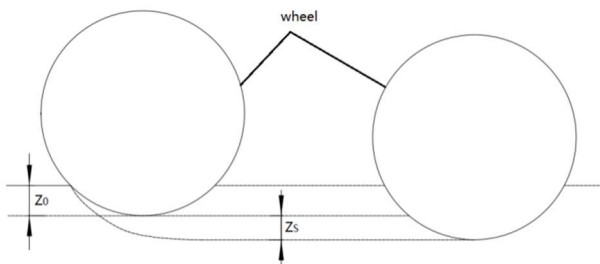

FIGURE 12. Schematic illustration of wheel subsidence.

Note: Z_0 is static settlement, mm; Z_S is dynamic settlement, mm.

The sinkage Z consists of two parts: the static sinkage Z_0 caused by soil compaction deformation and the sliding sinkage Z_s caused by soil shear deformation. That is:

$$Z = Z_0 + Z_s \qquad (23)$$

According to the Wong-Reece slip subsidence model (Chi et al., 2016), it can be concluded that

$$\begin{cases} Z_0 = [\frac{3W}{(k_c + bk_\phi)(3-n)\sqrt{D}}]^{\frac{2}{2n+1}} \\ Z_s = \frac{D}{2}(1-S)\theta_m \end{cases} \qquad (24)$$

According to (20) and (21), the contact stress σ and τ were relate to the soil parameters and structure parameters of the wheel such as the wheel entry angle θ_1, wheel departure angle θ_2, maximum stress angle θ_m, wheel radius r, and wheel width b. Owing to the uncertainty of the wheel soil contact process, the wheel soil contact stress changes continuously during the motion of the wheel.

Mechanical properties of wheel-soil contact

The walking speed is not high in the field operation, and the force and moment in the process of contact between the wheel and soil were balanced. It can be obtained that:

Especially, $S = (\omega r - v)/v$ $\qquad (25)$

in which:

D — the wheel diameter, mm;

ω — the angular velocity of the wheel, rad/s;

v — the driving speed of the wheel, m/s,

S — the wheel slip ratio.

Substituting (25) into (24), it can be deduced that:

$$Z = [\frac{3W}{(k_c + bk_\phi)(3-n)\sqrt{D}}]^{\frac{2}{2n+1}} + \frac{D}{2}(1-S)\theta_m \qquad (26)$$

According to the above analysis of the driving torque T, wheel load W, and sinkage Z, the factors influencing the wheel trafficability are the soil properties, wheel structure, and wheel driving speed.

Discrete element simulation experiment

The wheel-soil simulation model is established using the discrete element simulation software EDEM2.7. The traction of the rear wheel and surface flatness of the paddy are used as the evaluation index to simulate the working conditions of the weeder, and the mechanical characteristics of the wheel and soil are explored when the wheel and soil interact.

Soil particle model

According to the characteristics of paddy soil, it is divided into topsoil and subsoil (Bahrami et al., 2020). The topsoil is loose, whereas the subsoil is compact. Particularly, 0–150 mm is the topsoil, and 150–300 mm is the subsoil. According to the relevant literature (Ding et al., 2017; Li et al., 2019), the basic parameters of paddy soil are

as follows: the density, Poisson's ratio, and shear modulus of the topsoil are 1280 kg/m³, 0.36 and 6×10⁷ Pa, respectively, whereas those of the subsoil are 1500 kg/m³, 0.3, and 1×10⁸ Pa, respectively.

In the discrete element simulation, the reduction of the particle size leads to a significant increase in the simulation time. To reduce the simulation time, the particle size used in the discrete element simulation is generally larger than the actual size (Hao et al., 2019; Fang et al., 2016). Therefore, spherical particles with a radius of 8 mm were used as the soil particles. Hertz Mindlin with JKR is a cohesive contact model, which can embody the influence of van der Waals force in the contact area, and can better simulate the mechanical behavior of wet particles. This study will use this model to study the paddy soil particle model (Perni & Prokopovich 2015; Ciavarella 2018; Xiang et al., 2019).

Wheel model

To improve the simulation efficiency, the structure of the rear wheel of the weeder is simplified. The DEM software, EDEM, models the complex parts with difficulty, hence, the drawing software UG was used to build the three-dimensional model of the rear wheel of the weeder; the built three-dimensional model was then imported into the EDEM software in .igs format, and the material was set as rubber. Figure 13 is the simplified three-dimensional model of the rear wheel of the weeder. According to the operation in the field, the driving speed of the machine is set at 0.6 m/s.
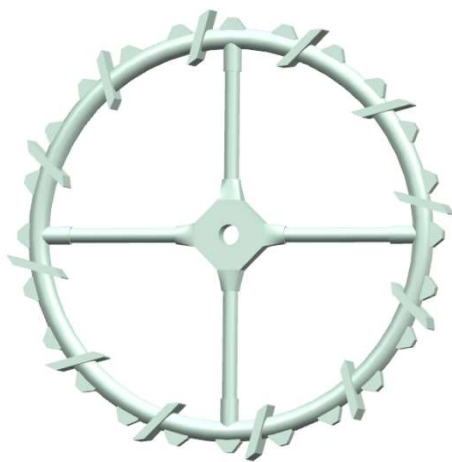

FIGURE 13. Schematic diagram of the rear wheel of the weeding machine.

Wheel soil interaction model

In this study, EDEM is used to simulate the interaction between the driving wheel and paddy soil during weeding. The virtual soil bin with length × width × height of 3,000 mm × 300 mm × 300 mm was established; subsequently, the single wheel virtual soil bin simulation test was carried out. At the beginning of the simulation, the subsoil particles were generated in the virtual soil bin, and the topsoil particles were generated above the subsoil particles after the generation of the subsoil particles was stable. Finally, the driving wheel of the weeder moves until the simulation is completed. According to the field observation, to fit the working condition and simulate the sinking of the wheel, the driving wheel of the weeder

penetrated 20 mm below the subsoil at the beginning of the simulation.
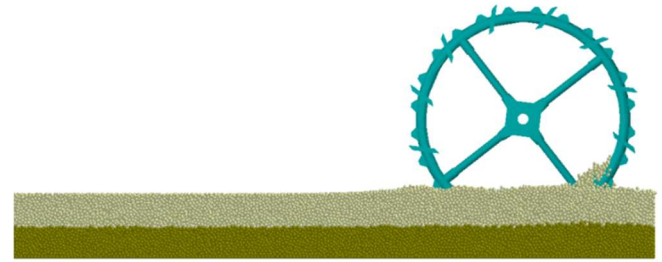

FIGURE 14. Diagram of wheel-soil interaction process.

Field performance experiment

To test the performance of the steering system of the paddy field weeder and verify the accuracy of the simulation test, the performance test of the paddy field weeder was carried out.

Test conditions

In July 2020, the field performance test of the paddy field weeder was carried out in Fenghuang Town, Fengtai County, Huainan City, Anhui Province. The experimental area was a rice wheat rotation field, the depth of the topsoil was 1500 mm, the depth of the water layer was 30 mm, and the temperature was 28~32℃. The main test equipment included the self-developed rear riding three wheels paddy field weeder prototype, a stopwatch (±0.1 s), tape measure (±1 mm), goniometer (0-360 mm, ±0.1º), and so on. The field test of the self-propelled system of the weeder is shown in Figure 15.

(a) Driving speed measurement

(b) Turning radius measurement

FIGURE 15. Field experiment of walking steering system of the weeding machine.

Test method

To verify the operation performance of the paddy field weeder self-propelled system, the turning radius, tipping angle, ridge height, and driving speed were selected as indexes to evaluate the steering ability, stability, obstacle crossing ability, and driving ability of the paddy field weeder self-propelled system. According to GB/T5667-2008 (agricultural machinery production test method) and the requirements of paddy field operation machinery (Wang et al., 2017 c), the self-propelled system of the rear mounted three wheels paddy field weeder was tested. The test methods of each index are as follows:

a) Turning radius: when the weeder enters the field, select the lowest operating speed, adjust the steering wheel to the limit position, and use a tape measure to measure the radius of the rutting track left by the machine when turning in the field. To reduce the test error, under the same working condition, the average value of the three measurements is taken as the minimum turning radius of the steering system of the paddy field weeder.

b) Limit tipping angle: under the condition of no wind or breeze, select the ramp close to the expected maximum climbing angle of the machine, and the weeder climbs at the lowest walking speed. If the machine can climb the ramp smoothly, choose a larger and steeper ramp to test. The maximum gradient that a weeder can climb is the ultimate tipping angle.

c) Ridge height: in the condition of no wind or breeze, select the ridge similar to the maximum ridge height calculated for the machine, and the weeding machine will cross the ridge with the lowest walking speed. If the machine can smoothly cross the ridge, then select a higher ridge for testing. The highest ridge height that the weeder can cross is the maximum ridge crossing height.

d) Driving speed: to measure the actual speed of the field operation and road driving of the weeder, a paddy field and flat road with a length of more than 100 m are selected respectively, and the operation area is divided into the acceleration start area, uniform speed test area, and braking deceleration area. The acceleration start area and braking deceleration area are 20 m, respectively. The test is started from the lowest speed gear, and the time required for the weeder to pass the operation area is recorded. Increase the speed by one gear at a time to check the speed range of the weeder.

RESULTS AND DISCUSSION

Discrete element simulation results

According to the characteristics of the soil structure and the mechanism of the wheel soil interaction, the traction of the rear wheel and surface flatness of a paddy are taken as test indexes to analyze the simulation test.

Wheel traction is an intuitive reflection of the road trafficability of the machine. The greater the wheel traction, the stronger the ability of the machine to accelerate uphill and overcome the uneven road in the field, and the stronger the road trafficability of the machine. Paddy soil is soft road; after the operation in the field, the machine damages the surface of the paddy field, which affects the growth of crops in the field and the subsequent operation of the machine. The surface flatness of paddy is the macroscopic performance of the road smoothness after the field

operation, and it is the comprehensive embodiment of the disturbance of paddy soil and the rheological characteristics of soil itself. The smaller the surface flatness, the smoother the road surface, and the smaller the impact on the growth of crops and the subsequent operation of machines.

Simulation results of wheel traction

Figure 16 shows the curve of the wheel traction force changing with time in the simulation test. In this study, the stable driving stage of the wheel in the soil trough is selected for analysis. The wheel enters the stable driving stage in approximately 5 s; at this time, the wheel traction gradually increases, and tends to be stable at approximately 600 N. The wheel traction presents fluctuation in a range. Subsequently, the wheel leaves the soil bin, and the traction force decreases gradually.
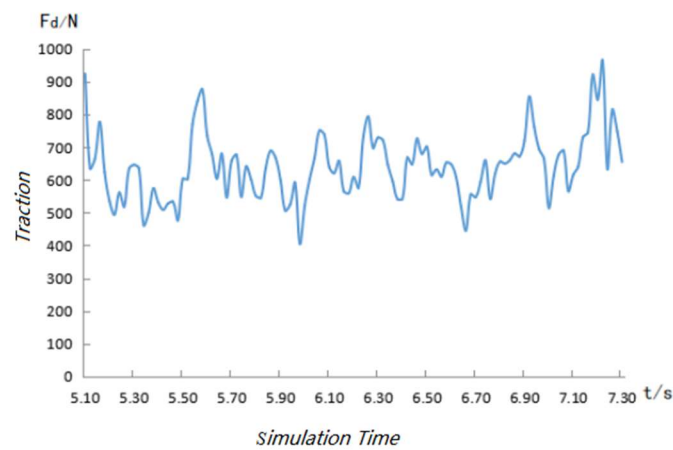

FIGURE 16. Diagram of traction-time line chart.

The wheel is equipped with a series of protrusions and wheel spines. When working in the field, the protrusions and wheel spines penetrate into the subsoil, which enhances the grip of the wheel, improves the adhesion, reduces the slip rate, and improves the traction efficiency. Figure 17 is the simulation test diagram of the driving wheel of the weeder after walking in the paddy soil. In figure 17, when the wheel passes the ground, the wheel spines break the subsoil, forming a series of small pits. Subsequently, the small pit was filled by the upper layer of the mobile flooded soil. The gripping force of the wheel to the soil is significantly improved, which effectively reduces the wheel slip.

FIGURE 17. Simulation of wheel-soil interaction result.

Simulation results of surface flatness

The simulation cross section of the wheel after walking in the paddy field is shown in Figure 18. Scale a is the datum line of the highest point of the paddy field surface, and scale b is the datum line of the lowest point of the paddy field surface. The distance between scale a and scale b is 30 mm, which means that the surface flatness is less than 30 mm after the simulation operation.
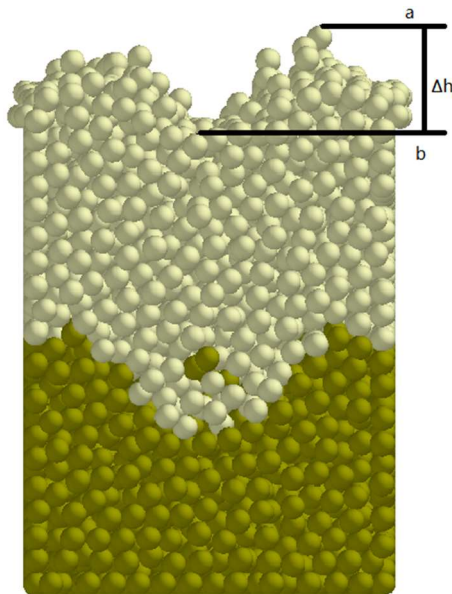
FIGURE 18. Simulation result of surface smoothness.

Note: a is scale a; b is scale b; Δh is the distance between scale a and scale b, mm.

Field test results and analysis

The performance test results of the weeder self-propelled system are presented in Table 1.

TABLE 1. Results of performance test.

Testing Parameters	Technical Requirements	Testing results
Minimum turning radius (mm)	≤3500	2,050
Maximum climbing ridge angle (°)	≥30	36
Maximum climbing ridge height (mm)	≥300	400
Driving speed （km/h）	0~14	0.72~16.20

The field performance test results show that the minimum turning radius of the designed paddy field weeder is 2,050 mm, which is less than the turning radius of the four wheels machine, and meets the requirements of the paddy field working environment for the turning radius of the machine. In the test area, the ultimate turning angle of the prototype is 26º, the maximum height over the ridge is 400 mm. The speed range of the weeder in the driving gear is 0.72~16.20 km/h, and the speed range in the weeding gear is 0.72~5.40 km/h, which meet the speed requirements of the weeder in road driving and field operation.

In the field test, there are machine slip and human error, and the results of the field test are slightly different from the theoretical analysis. Due to wheel slip of weeding device and imperfect driving of test personnel, the turning radius of weeding machine is larger than the theoretical analysis value. During operation, due to the uneven field road and loose soil, the maximum climbing ridge angle and maximum climbing ridge heigh are lower than the theoretical analysis value. The results of field experiment

and theoretical analysis are generally consistent, which proves the feasibility of the method used in this study.

Owing to the complex working environment of the paddy field, the performance indexes measured are not fixed and change according to different conditions, but they all meet the technical requirements of the paddy field management. The overall performance of the self-propelled system can meet the requirements of field weeding and road transportation.

Discussion

(1) When the wheel runs stably in the soil trough, the traction of the wheel is approximately 600 N. The paddy soil is divided into topsoil and subsoil. The subsoil is compact, whereas the topsoil is loose. When the machine is working in the field, the wheels move on the subsoil to stir the topsoil. The topsoil is loose and is formed after irrigation and soaking. When the wheels drive past, owing to the high mobility of the soil and the low friction between the wheels and soil, the wheel grip is not enough and it is easy to slip, which affects the performance of the weeder. In this study, there are protrusions and spikes on the outer edge of the wheel. When the weeder is working in the field, the protrusions and spikes on the wheel pierce the subsoil, which increases the wheel grip, reduces the slip phenomenon, and ensures the wheel traction.

(2) After driving, the flatness of the paddy field surface is less than 30 mm. When the weeder is working in the field, the protrusions and wheel spines penetrate into the subsoil, and the wheels stir the soil and discharge the mud around to form a series of soil pits. Owing to the fluidity of the soil in the flooded layer, the series of soil pits left by the wheels should be filled to keep the paddy field flat.

CONCLUSIONS

The self-propelled system of the three-wheel paddy field weeder was designed, and the design requirements, overall structure and working principle were illustrated.

(1) This research analyzes the factors influencing the trafficability of the self-propelled walking system for the paddy field weeder, explores the interaction mechanism of the wheel soil during the operation of the weeding machine, and determines the structure parameters of the system according to the analysis results.

(2) This research established the wheel soil interaction discrete element simulation model. The wheel traction and surface flatness were used as the test indices to simulate the soil bin of a single wheel. The change of the wheel traction and influence of the wheels on the surface of the paddy field were analyzed. The results show that the traction force of the wheels is approximately 600 N and the surface flatness is less than 30 mm during the interaction.

(3) The field experiment was carried out with the turning radius, driving speed, climbing angle, and ridge height of the mower walking system as the test indices. The experimental results show that the minimum turning radius of the weeder is 2,050 mm, the ultimate turning angle is 36°, the maximum height of the crossing ridge is 400 mm, the speed range of the mower in the road driving gear is 0.72–16.20 km/h, and the speed range in the gear of weeding operation is 0.72–5.40 km/h. The system designed in this study can meet the field weed control requirements.

ACKNOWLEDGEMENTS

REFERENCES

Atul RD, Birbal S, RK Naik, Devchand S (2017) Optimizing the profits and enhancing productivity of rice through mechanization. International Journal of Agricultural Engineering 10(2): 331-336

Bahrami M, Naderi-Boldaji M, Ghanbarian D, Ucgul M, Keller T (2020) Simulation of plate sinkage in soil using discrete element modelling: Calibration of model parameters and experimental validation. Soil and Tillage Research 203(104700). DOI: https://doi.org/10.1016/j.still.2020.104700

Bai H, Yin C (2017) Effects of different seedling raising methods on seedling quality, plant morphology and yield of rice. China Rice 23(5): 92-93. DOI: https://doi.org/10.3969/j.issn.1006-8082.2017.05.025

Bao Y, Yang J, Zhao Y, Liu X, Guo Y, Li Z, Xiang J (2020) Design of the walking driving system for a blueberry harvester based on contact mechanical behavior of wheel-soil. Transactions of the Chinese Society of Agricultural Engineering 36(7): 43-52. DOI: https://doi.org/10.11975/j.issn.1002-6819.2020.07.005

Basavaraj A, Surendrakumar C, Divaker D (2016) Study of agronomical and soil parameters in paddy field for development of paddy weeder. International Journal of Agricultural Sciences 8(30): 1627-1631

Chen B, Zou M, Dang Z, Huang H, Jia Y, Shi R, Li J (2019) Experiment on pressure-sinkage for mesh wheels of CE-3 lunar rover on lunar regolith. Journal of Jilin University (Engineering and Technology Editon) 49(06): 1836-1843. DOI: https://doi.org/10.13229/j.cnki.jdxbgxb20180904

Chen S, Zhang S, Sun X, Li Y (2012) Design and experiment of self-propelled high-ground-clearance spreader for paddy variable-rate fertilization. Transactions of the Chinese Society of Agricultural Engineering 28(11): 16-21. DOI: https://doi.org/10.3969/j.issn.1002-6819.2012.11.003

Chi Y, Zhang R, Ren J, Li H, Wang Y (2016) Steering power ratio affected by soil sinkage with differential steering in tracked vehicle. Transactions of the Chinese Society of Agricultural Engineering 32(17): 62-68. DOI: https://doi.org/10.11975/j.issn.1002-6819.2016.17.009

Ciavarella M (2018) An approximate JKR solution for a general contact, including rough contacts. Journal of the Mechanics and Physics of Solids 114: 209-218. DOI: https://doi.org/10.1016/j.jmps.2018.03.005

Ding Q, Ren J, Belal AE, Zhao J, Ge S, Li Y (2017) DEM Analysis of Subsoiling Process in Wet Clayey Paddy Soil. Transactions of the Chinese Society for Agricultural Machinery 48(03): 38-48. DOI: https://doi.org/10.6041/j.issn.1000-1298.2017.03.005

Editorial Department of China Journal of highway and transport (2016) Review on China's traffic engineering research progress: 2016. China Journal of Highway and Transport 29(06): 1-161. DOI: https://doi.org/10.19721/j.cnki.1001-7372.2016.06.001

Fang H, Ji C, Zhang Q, Guo J (2016) Force analysis of rotary blade based on distinct element method. Transactions of the Chinese Society of Agricultural Engineering 32(21): 54-59. DOI: https://doi.org/10.11975/j.issn.1002-6819.2016.21.007

Fu T (2018) Research on driving anti-skid control technology of paddy field self-propelled sprayer. Master Thesis, Chinese Academy of Agricultural Mechanization Sciences.

Ge J, Zhan D, Wang X, Cao C, Fang L, Duan M (2019) Tractive performances of single grouser shoe affected by different soils with varied moisture contents. Advances in Mechanical Engineering 11(5): 1-11. DOI: https://doi.org/10.1177/1687814019849133

Hao J, Long S, Li H, Jia Y, Ma Z, Zhao J (2019) Development of discrete element model and calibration of simulation parameters for mechanically harvested yam. Transactions of the Chinese Society of Agricultural Engineering 35(20): 34-42. DOI: https://doi.org/10.11975/j.issn.1002-6819.2019.20.005

Hao Z, Yang X, Liu L, Yin S, Liu S, Zhao J (2018) Design and experiment of multifunctional dynamic chassis for orchard. Transactions of the Chinese Society for Agricultural Machinery 49(12): 66-73+92. DOI: https://doi.org/10.6041/j.issn.1000-1298.2018.12.008

He J, Li H, Chen H, Lu C, Wang Q (2018) Research progress of conservation tillage technology and machine. Transactions of the Chinese Society for Agricultural Machinery 49(04): 1-19. DOI: https://doi.org/10.6041/j.issn.1000-1298.2018.04.001

Huang H, Li J, Wu B, Zhang G, Xue L, Wang Y (2015) Construction and verification of lightweight vehicle wheel tractive trafficability model under light load. Transactions of the Chinese Society of Agricultural Engineering31(12): 64-70. DOI: https://doi.org/10.11975/j.issn.1002-6819.2015.12.009

Kwangseok O, Jaho S, Jin-Gyun K, Kyongsu Y (2017) MPC-based approach to optimized steering for minimum turning radius and efficient steering of multi-axle crane. International Journal of Control, Automation and Systems 15(4). DOI: https://doi.org/10.1007/s12555-015-0472-6

Li J, Huang H, Wang Y, Tian L, Ren L (2015) Development on research of soft-terrain machine systems. Transactions of the Chinese Society for Agricultural Machinery 46(05): 306-320. DOI: https://doi.org/10.6041/j.issn.1000-1298.2015.05.044

Li J, Tong J, Hu B, Wang H, Mao C, Ma Y (2019) Calibration of parameters of interaction between clayey black soil with different moisture content and soil-engaging component in northeast China. Transactions of the Chinese Society of Agricultural Engineering 35(6): 130-140. DOI: https://doi.org/10.11975/j.issn.1002-6819.2019.06.016

Li N, Chen Z, Zhu C, Zhang C, Sun Z, Li W (2016) System design and experiment of electric driven weeding robot. Transactions of the Chinese Society for Agricultural Machinery 47(05): 15-20 + 69. DOI: https://doi.org/10.6041/j.issn.1000-1298.2016.05.003

Ma X, Qi L, Liang B, Tan Z, Zuo Y (2011) Present status and prospects of mechanical weeding equipment and technology in paddy field. Transactions of the Chinese Society of Agricultural Engineering 27(6): 162-168. DOI: https://doi.org/10.3969/j.issn.1002-6819.2011.06.030

Perni S, Prokopovich P (2015) Multi-asperity elliptical JKR model for adhesion of a surface with non-axially symmetric asperities. Tribology International 88: 107-114. DOI: https://doi.org/10.1016/j.triboint.2015.03.001

Qi L, Liang Z, Ma X, Tan Y, Jiang L (2015) Validation and analysis of fluid-structure interaction between rotary harrow weeding roll and paddy soil. Transactions of the Chinese Society of Agricultural Engineering 31(5): 29-35+37+36. DOI: https://doi.org/10.3969/j.issn.1002-6819.2015.05.005

Qi L, Liang Z, Yu J, Ma X, Wu T, Lu Y, Zhao L (2016) Design and field test of lightweigh paddy weeder. Joural of Jilin University (Engineering and Technology Editon) 46(03): 1004-1012. DOI: https://doi.org/10.13229/j.cnki.jdxbgxb201603048

Qi L, Liao W, Ma X, Lin J, Ou Z, Zhan Z (2013) Design and testing of control system of mini-weeding-robot platform in rice paddy field. Journal of Jilin University (Engineering and Technology Edition) 43(04): 991-996. DOI: https://doi.org/10.7964/jdxbgxb201304024

Qi L, Ma X, Tan Z, Tan Y, Qiu Q, Yang C, Zhang W (2012) Development and experiment of marching-type inter-cultivation weeder for paddy. Transactions of the Chinese Society of Agricultural Engineering 28(14): 31-35. DOI: https://doi.org/10.3969/j.issn.1002-6819.2012.14.005

Qi L, Zhao L, Ma X, Cui H, Zheng W, Lu Y (2017) Design and test of 3GY-1920 wide-swath type weeding-cultivating machine for paddy. Transactions of the Chinese Society of Agricultural Engineering 33(8): 47-55. DOI: https://doi.org/10.11975/j.issn.1002-6819.2017.08.006

Qin W, Geng Q, Huang Y, Du L, Zhang W (2014) Analysis and optimization of Macpherson steering suspension. Transactions of the Chinese Society for Agricultural Machinery 45(10): 15-21. DOI: https://doi.org/10.6041/j.issn.1000-1298.2014.10.003

Sun Z, Tang L, Wang W, Zhao J, Shen C, Sun Y (2017 a) Flexible track stress distribution considering slip subsidence. Transactions of the Chinese Society for Agricultural Machinery 48(01): 317-324. DOI: https://doi.org/10.6041/j.issn.1000-1298.2017.01.042

Sun Z, Zhang C, Ma Y, Zhang G, Li W, Tan Y (2017 b) Optimal design and experiment of thinning hoe for swing motion thinning robot. Transactions of the Chinese Society for Agricultural Machinery 48(09): 70-75. DOI: https://doi.org/10.6041/j.issn.1000-1298.2017.09.009

Tang L, Hu L, Zang Y, Luo X, Zhou H, Zhao R, He J (2018) Method and experiment for height measurement of scraper with water surface as benchmark in paddy field. Computers and Electronics in Agriculture 152:198-205. DOI: https://doi.org/10.1016/j.compag.2018.07.020

Tao G, Wang J, Zhou W, Niu C, Zhao J (2015) Herbicidal mechanism and key components design for paddy weeding device. Transactions of the Chinese Society for Agricultural Machinery 46(11): 57-63. DOI: https://doi.org/10.6041/j.issn.1000-1298.2015.11.009

Tian L, Cao C, Qin K, Fang L, Ge J (2021) Design and test of post-seat weeding machine for paddy. International Journal of Agricultural and Biological Engineering 14(3):112-122. DOI: 10.25165/j.ijabe.20211403.5936

Wang J, Li C, Li X, Li X, Wang J (2018) Design and experiment of 3SCJ-1 type weeding machine for paddy field applied to film mulching and transplanting. Transactions of the Chinese Society for Agricultural Machinery 49(04): 102-109. DOI: https://doi.org/10.6041/j.issn.1000-1298.2018.04.012

Wang J, Tang H, Shen H, Bai H, Na M (2017 a) Design and experiment of high clearance roll-waist multifunctional power chassis for paddy field. Transactions of the Chinese Society of Agricultural Engineering 33(16): 32-40. DOI: https://doi.org/10.11975/j.issn.1002-6819.2017.16.005

Wang J, Wang J, Yan D, Tang H, Zhou W (2017 b) Design and experiment of 3SCJ-2 type row weeding machine for paddy field. Transactions of the Chinese Society for Agricultural Machinery 48(06): 71-78+202. DOI: https://doi.org/10.6041/j.issn.1000-1298.2017.06.009

Wang Q, Gao Z, Yao C, Zhang J, Chang B, Gao P, Liu F (2017 c) Relationship between subsoil properties of paddy field and rice root growth in Northeast China. Chinese Journal of Soil Science 48(1): 177-181. DOI: https://doi.org/10.19336/j.cnki.trtb.2017.01.22

Wang Z, Ding X, Zhang L (2019) Overview on key technologies of acceleration slip regulation for four-wheel-independently-actuated electric vehicles. Journal of Mechanical Engineering 55(12): 99-120. DOI: https://doi.org/10.3901/JME.2019.12.099

Xiang W, Wu M, Lv J, Quan W, Ma L, Liu J (2019) Calibration of simulation physical parameters of clay loam based on soil accumulation test. Transactions of the Chinese Society of Agricultural Engineering 35(12): 116-123. DOI: https://doi.org/10.11975/j.issn.1002-6819.2019.12.014

Xie X, Gao F (2016) Tractive performance analysis of transformable wheel on soft terrain. Transactions of the Chinese Society for Agricultural Machinery 47(S1): 457-463. DOI: https://doi.org/10.6041/j.issn.1000-1298.2016.S0.069

Xue L, Dang Z, Chen B, Li J, Zou M (2020) Advances and Prospects of Martian Soil parameter Identification Based on Terramechanics. Journal of Astronautics 41(02): 136-146. DOI: https://doi.org/10.3873/j.issn.1000-1328.2020.02.002

Zang L, Zhao Y, Li B, Chen Y, Li X (2014) Influence of mechanical elastic wheel configuration on traction performance. Journal of Harbin Engineering University 35(11): 1415-1421. DOI: https://doi.org/10.3969/j.issn.1006-7043.201312081

Zhang J, Chen D, Wang S, Hu X, Wang D (2015) Design and experiment of four-wheel independent steering driving and control system for agricultural wheeled robot. Transactions of the Chinese Society of Agricultural Engineering 31(18): 63-70. DOI: https://doi.org/10.11975/j.issn.1002-6819.2015.18.010

Zhao J, Wang W, Sun Z, Su X (2016) Improvement and verification of pressure-sinkage model in homogeneous soil. Transactions of the Chinese Society of Agricultural Engineering 32(21): 60-66. DOI: https://doi.org/10.11975/j.issn.1002-6819.2016.21.008

Zhu M, Xing Z, Wu P, Qian H, Cao W, Hu Y, Guo B, Wei H, Xu K, Huo Z, Dai Q, Zhang H (2017) Effects of sowing method and planting density on yield and photosynthetic production of carpet seedling machine transplanting rice. China Rice 23(6): 84-87. DOI: https://doi.org/10.3969/j.issn.1006-8082.2017.06.019